CrossMark

Structural and electrical characteristics of barium modified bismuth-sodium titanate $(Bi_{0.49}Na_{0.49}Ba_{0.02})TiO_3$

Sugato Hajra[1] · Sushrisangita Sahoo[2] · Manojit De[3] · Pravat Kumar Rout[1] · H. S. Tewari[3] · R. N. P. Choudhary[2]

Abstract The lead-free polycrystalline ceramic, barium titanate modified bismuth–sodium titanate 0.98 $(Bi_{0.5}Na_{0.5}TiO_3)$ + 0.02 $BaTiO_3$ (BNT–BT-2) was synthesized by using a mixed oxide route at high temperature. The structural (crystal structure, microstructure, molecular structure), and electrical (dielectric constant and loss, impedance, conductivity) characteristics of the parent compound $(Bi_{0.5}Na_{0.5}TiO_3)$ have greatly been influenced by the addition of even a small amount of barium titanate in it. Preliminary structural study of BNT–BT-2 using X-ray diffraction data clearly shows the formation of a single-phase perovskite structure with the coexistence of hexagonal (major phase) and tetragonal (minor) phases. The existence of diffuse phase transtition and the relaxor behaviour in the material is confirmed by analysis of temperature-frequency dependence of dielectric parameters. The composition $(0.98BNT - 0.02BT)$ of the material shows non-Ohmic conduction in its J–E characteristics. In this lead-free ceramic, permittivity anomalies are matched to modulus anomalies. The highlighted features are determined by structural phase transitions of the ferroelectric-like.

✉ Pravat Kumar Rout
pkrout_india@yahoo.com

1 Department of Electrical and Electronics Engineering, Siksha O Anusandhan University, Bhubaneswar, India

2 Department of Physics, Siksha O Anusandhan University, Bhubaneswar, India

3 Department of Pure and Applied Physics, Guru Ghasidas Central University, Bilaspur, India

1 Introduction

A solid solution of lead zirconate and lead titanate $(PbZrO_3–PbTiO_3,$ known as PZT) near the morphotropic phase boundary (MPB) is widely used for different applications (sensors, actuators, printing devices, micropositioning systems) due to its exceptional electromechanical and piezoelectric properties. As lead or lead oxide released during the high-temperature processing of the PZT is toxic in nature, it creates severe health and environmental problems. Keeping in mind the environmental concerns, serious attempts are being made to develop lead-free ferroelectric, piezoelectric and related materials having potential device characteristics (i.e., low dielectric loss, low coercive field, low conductivity, high dielectric constant and large saturation potential) [1–3]. PZTs, $BaTiO_3$, $BaSrTiO_3$, $KNbO_3$, $(Bi_{1/2}Na_{1/2})TiO_3$, etc. are closely associated with perovskite structure exhibiting co-existence of multiphases [4–6]. Basically, the above lead-free piezoelectric ceramics have low piezoelectric coefficients (d_{33}) (less than 300 pC/N) as compared to that of the PZT $(d_{33} = 300–600$ pC/N) [7–9]. The electric properties studied by many researchers of these materials are not still uniform and intact [10, 11]. The variety of solid solutions related to $(Bi_{1/2}Na_{1/2})TiO_3$ (BNT) modified with (i) $BiFeO_3$ [12], (ii) $CaTiO_3$ [13], (iii) $BaTiO_3$ [14] were experimented to enhance their electrical characteristics. Most of the past investigations show two phase transitions at high temperatures (530 °C: paraelectric cubic phase to paraelectric tetragonal phase) and at low temperature (200 °C: ferroelectric rhombohedral phase is present). Due to the existence of a rhomobohedral- tetragonal MPB around x = 0.06–0.07, among all BNT–BT systems studied, $(Bi_{1/2}Na_{1/2})_{1-x}Ba_xTiO_3$ (x = concentration) have attracted lots of attention [15]. Still, the steady results are far with an approach to device engineering as per the electric characteristics of BNT–BT solid

solutions are concerned [16–19]. To enhance any specific characteristics, BNT is regarded to be an excellent material. As the structural and electrical characterization of BNT–BT with 2 wt% of BT reports are not available, we have made the A-site and B-site substitutions in BNT to analysis the relaxor properties, phase transitions and related properties of the material [20]. In the present work, the influence of even a small amount (2 wt%) of Ba^{2+} ions on physical and electrical properties of BNT ceramics at the morphological phase boundary has systematically been investigated and reported here.

2 Experimental

2.1 Synthesis of BNT–BT-2

The high-purity ingredients/oxides used here are; bismuth oxide [purity = 99.99%, Central drug house (P) LTD], sodium carbonate (purity = 99.5%, Central drug house (P) LTD), barium carbonate [purity = 99.99%, Central drug house (P) LTD], titanium oxide [purity = 99.99%, LobaChemie (P) LTD]. A conventional and standard mixed oxide route (i.e., high-temperature solid-state reaction method) has been used for the synthesis of the desired material. The ingredient materials were properly taken in stochiometry, and were grounded in agate mortar. Dry grinding was followed by wet grinding (acetone) for 4 h each. The calcination of the homogeneously mixed powder was carried out at 850 °C for 12 h in a high temperature heat furnace. The fine calcined powder was sieved for fabrication of disc-shaped pellets of 10 mm diameter of varying thickness under isostatic pressure of 4×10^6 Nm^{-2}. The binder used was PVA for fabrication of pellets. The pellets were sintered for 6 h at an optimized temperature of 950 °C.

2.2 Characterization

The X-ray diffraction data and pattern, obtained by X-ray diffractometer (Bruker D-8 advance model) with CuKα (λ = 0.15406 nm) in a wide range of Bragg's angle (20° ≤ 2θ ≤ 80°), were used to study the formation and crystalline nature of the prepared material. Analysis of Raman spectra recorded at room temperature by using STR-500 Micro Raman, Japan was carried out to understand the molecular structure and symmetry. The surface characteristics (grain size, shape, distribution, etc.) of a pellet sample were analysis using micrograph obtained by scanning electron microscope (SEM) of M/s CARL ZEISS. The elemental analysis was carried out by energy dispersion analysis of X-ray (EDAX) using the same SEM micrograph. The color mapping and distribution of elements of the sample were performed by Oxford

instruments, Japan. Both the surfaces of the pellet were polished with fine emery paper to make them smooth and parallel. The high-purity silver paste was subsequently painted on the parallel surface of the pellet, and then was annealed in an oven at 120 °C for 2 h to remove moisture, if any. The phase sensitive LCR or impedance meter (model PSM 1735, N4L), in a wide range of frequency (1 kHz–1 MHz) and temperature (25–500 °C), was used to obtain electrical parameters such as relative permittivity, energy dissipation factor, electrical impedance (Z), conductivity and modulus. A digital multimeter was used to measure the temperature. The J–E curve was measured by using a keithley electrometer at a frequency of 50 Hz.

3 Results and discussion

3.1 Structure and microstructural analysis

The X-ray diffraction (XRD) pattern (Fig. 1a) was used to investigate the structural characteristics of the material (BNT–BT-2). To get the detail structural information of the sample, Rietveld refinement was carried out using the patterns and software PDXL. The Rietveld refinement fitting results are shown in Fig. 1b. Based on best fitting parameters ($R_{wp} \approx 10.43$, $R_p \approx 8.08$, $\chi^2 \approx 1.5687$), all the peaks are indexed with a very well matched (the fitted data i.e. blue line exactly match with experimental data i.e. red line) hexagonal phase [space group file number = 166: (R-3m); ICDD Card No. 04-015-0482]. There is an extra peak present at $2\theta \approx 31°$ which corresponds to the tetragonal phase (space group 139: I4/mmm; ICDD Card No. 04-010-5863). The XRD pattern was fitted with whole powder pattern fitting (WPPF) analysis. The lattice parameters have also been estimated by Rietveld method: a = b = 5.4867 Å and c = 6.7155 Å. Hence c/a ratio in this case is 1.22. The X-ray density of the sample was calculated by an available software PDXL2 (Rigaku, Japan) and found to be 7.683 gm/cc. Based on the structural data and the Goldsmith tolerance factor, a stable perovskite structure is concluded [21]. There is an increase in tetragonal distortion (c/a ratio) as compared to that of reported ones [22, 23]. A well known Debye–Scherrer equation: $D = p\lambda/\beta_{1/2}\cos\theta$ is utilized to calculate the crystallite size (D) of the sample where the reflection peak broadening is represented by ($\beta_{1/2}$), Bragg angle (θ) and wavelength (λ) respectively and p = constant (0.89). The calculated average value of D is found to be 100 nm. The morphology for one sample of BNT–BT-2 ceramic is shown as inset of Fig. 1b. It is visibly enumerated that the surface morphology is highly crystalline as enumerated from XRD analysis. The grain growth is not uniform, but confirms high density packing.
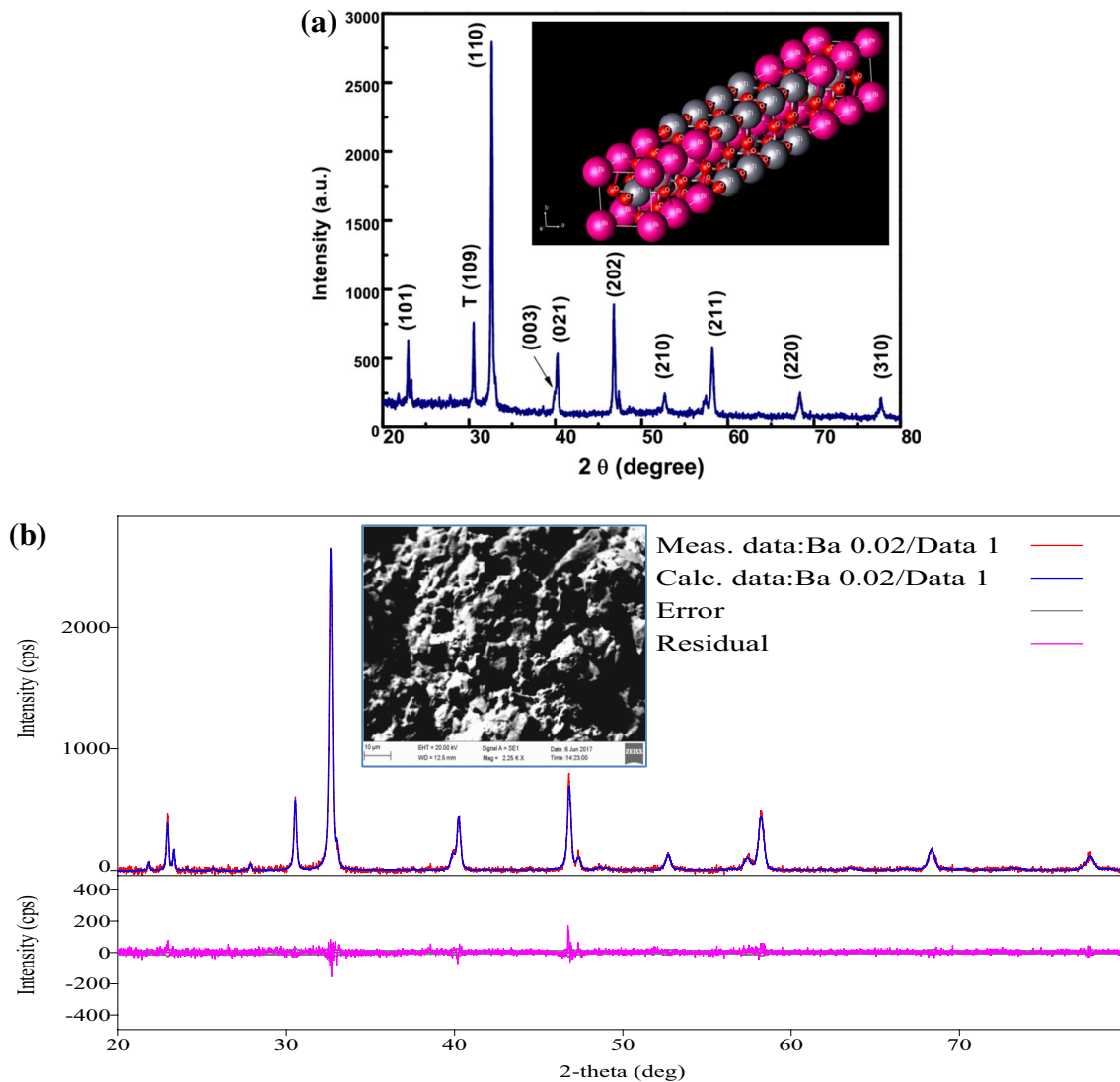
Fig. 1 a Room temperature XRD of BNT–BT-2 sample; Inset image shows unit cell structure of BNT–BT-2. **b** Rietveld refined pattern, inset SEM microstructure image

3.2 Elemental analysis and color mapping

Figure 2 shows the energy dispersive X-ray spectroscopy (EDX) spectra and elemental mapping of the sample which help to study the chemical composition or content of the prepared materials in the sintered ceramic sample. The presence and amount of bismuth, barium, sodium, titanium and oxygen ions of BNT–BT-2 sample have been obtained by EDX spectra. The analysis of the spectra shows that all the elements are homogeneously and proportionally distributed throughout the samples. Especially, the elements such as Bi, Na, Ba, Ti and O were seen to be homogeneously distributed across the grains and grain boundaries. The main purpose of the regional element mapping is to find out an insight among the grain and grain boundaries related to elemental distribution. The elemental ratios of the samples were nearly consistent with the required empirical formula.

3.3 Raman analysis

Figure 3 represents the room temperature Raman spectra of BNT–BT-2 recorded within the wavelength range from 132 to 900 cm^{-1}. Bands located below 250 cm^{-1} are related to Na/Bi–O stretching vibrations. The bands present above 250 cm^{-1} are mainly related to the Ti–O stretching vibrations. More specifically, the 269 cm^{-1} modes involves only O–Ti–O bending mode, which is susceptible to the phase transition [24]. The oxygen displacements (causing vibration) dominate the high-frequency Raman bands [25]. The high-frequency modes in the range of 600–850 cm^{-1}
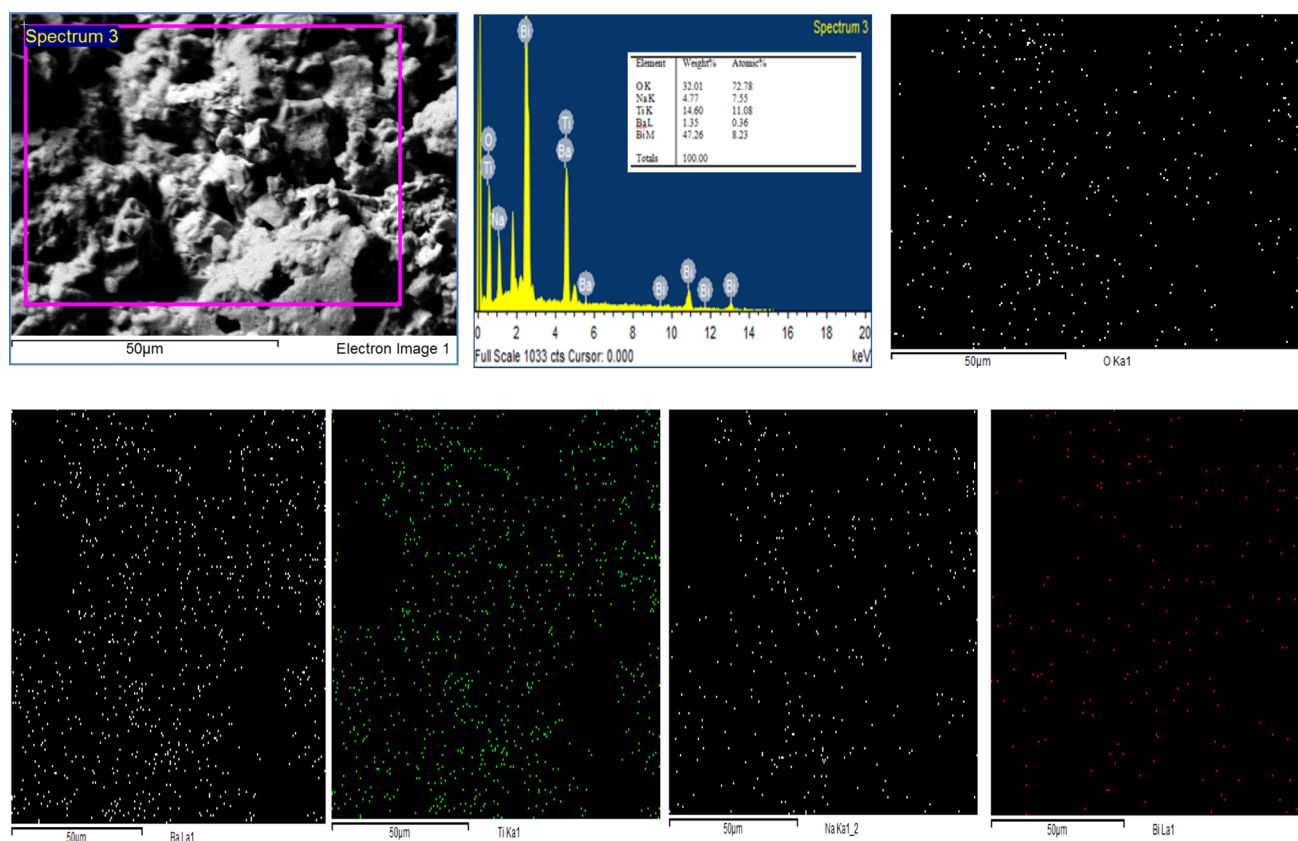
Fig. 2 EDS (Spectra and table (insert)); Elemental mapping of the BNTBT-2 samples at a marked region. All the constituent elements are present over the all surface
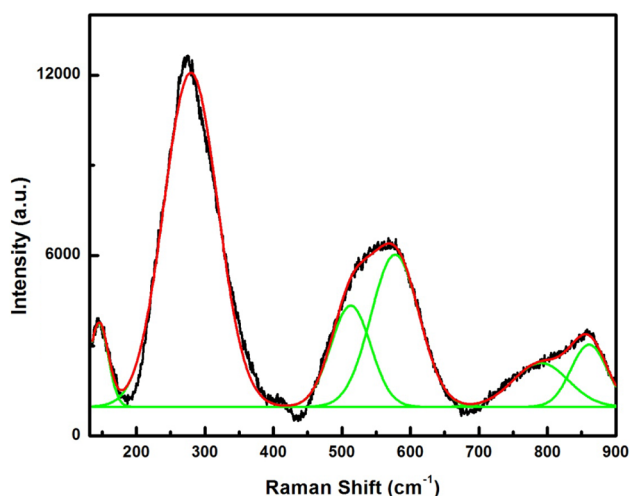

Fig. 3 Room temperature RAMAN spectra for BNT–BT-2

correspond to the vibrations of the TiO_6 oxygen octahedral [26]. The deconvolution of the spectrum, carried out by "Origin 8.0 software" using Lorentzian function, shows five vibrational modes observed at 269, 514, 581, 759 and

862 cm^{-1} which are in a good agreement with the previously reported ones [27, 28]. The distorted octahedral $[BiO_6]$ and $[NaO_6]$ clusters are closely associated with the first Raman-active A_1 (TO_1) mode at around (146 cm^{-1}). The second Raman active E (TO_2) mode at 269 cm^{-1} can be deconvoluted in three Raman peaks. Due the existence of octahedral $[TiO_6]$ clusters, this mode corresponds to stretching from the bonds. The third Raman-active (LO_2) mode with low intensity represents to short-range electrostatic forces because of iconicity of lattice. The TO_3 mode located around 581 cm^{-1} is attributed to the (–O–Ti–O–) stretching symmetric vibrations of the octahedral $[TiO_6]$ clusters [29]. This mode occurs commonly in the materials with perovskite structure. Finally, at 862 cm^{-1}, the (LO_3) mode is due to the existence of the sites within the rhombohedral lattice pre containing octahedral distorted $[TiO_6]$ clusters. The two classifications of the modes are longitudinal (LO) and transverse (TO) components. The reason behind such classification is due to the electronic structure with polar character of lattice. The Raman peaks are very prominent and detectable in BNT–BT ceramics. The distorted octahedral $[TiO_6]$ clusters is present, which provoked such behavior.

3.4 Analysis of dielectric parameters

Figure 4a, b shows the decrease in the dielectric parameters (permittivity and tan δ) with a rise in frequency. It can be observed that with increasing frequency (from the low-frequency), there is a rapid decrease in the dielectric constant, however, for higher frequency (> 10 kHz) it reaches a saturation limit. In the low-frequency region, dipolar polarization and space charge polarization participate most significantly to produce high dielectric constant [30]. The interfacial polarizations play an important role at low frequencies, but it was ineffective at higher frequency. The electronic polarization donates to the permittivity at high frequencies only. So, the low-frequency dielectric constant is greater as compared to that of higher frequency [31]. Due to the decrease of

permittivity on rising frequency, the dipoles fail to maintain the exact oscillatory field. The variation in permittivity can be observed in the wide temperature range.

The value of tan δ is observed very less (below 0.1) in the frequency region of 10^3–10^4 Hz. With an increase in frequency, the tan δ value decreases, as the charge carriers progress does not follow the applied field frequency above a certain range of frequency.

Figure 4c, d shows the temperature dependence of the dielectric parameters (permittivity and tan δ) at selected frequencies (1–500 kHz). T_d (depolarization temperature) and T_c are considered to be the two dielectric anomalies present in most BNT–BT based materials. Around 200 °C, as represented by T_d (depolarization temperature) shows the transition from ferroelectric to antiferroelectric whereas around
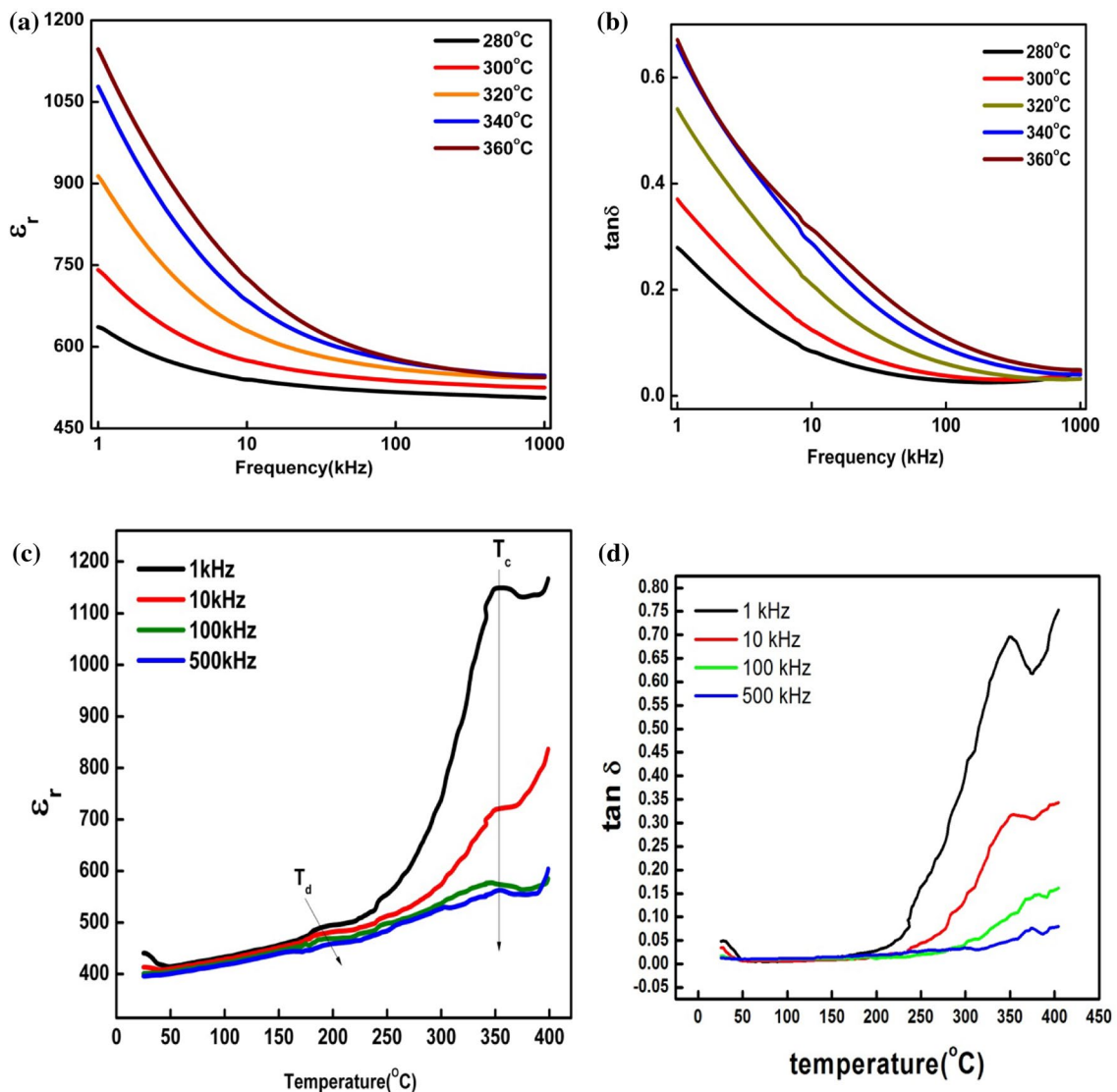

Fig. 4 **a** and **b** Shows (permittivity and tan δ) Increasing frequency at various temperature zones. **c** and **d** Temperature dependence of dielectric constant and loss at various frequencies (1–500 kHz)

340 °C (represented by T_c) (Curie temperature/maximum temperature) corresponds to the antiferroelectric to paraelectric phase transitions. In the tan δ vs. temperature curve, T_d is represented by the temperature of the first peak of tan δ whereas T_c is relatively broad suggesting a diffused phase transition [32, 33]. With a rise in the frequency, the two dielectric anomalies (T_d and T_c) move towards the higher temperature side representing the characteristics of typical relaxor behaviour (TRB). The TRB is determined by various phase transitions with the increasing shift of transition temperature with the rise in the frequency. The tan δ loss increases with rise in temperature caused when the dipole movement reaches maximum at a certain temperature.

3.5 AC conductivity analysis

Figure 5a, b exhibits the study of the electrical conduction mechanism which helps to understand the behaviour of charge carriers, temperature and field effect of the motion of charges and function of domain structure. The transport properties of the materials can also be examined by this analysis. The material processing conditions (calcinations and sintering temperature, time, atmosphere, etc) lead to the creation of oxygen vacancies, defects and charge carriers production in oxides together with perovskite is a well established fact [34]. From the AC conductivity vs. frequency graph, it is clearly seen that frequency dependence of AC conductivity is explained by an equation $\sigma_{AC} = A\omega^n$ where A corresponds to constant depending on temperature, ω represents to angular frequency and n as the frequency exponent. The value of n rises with an increase in the temperature, which represent a small polaron hopping model [35]. Thermal effect on the conductivity of the studied material at selected frequencies is illustrated in Fig. 5b. The

calculated value of the activation energy from slope was seen to enhance from 0.55 eV (1 kHz) to 0.68 eV (100 kHz) in the high-temperature region. The activation energies for the high temperature region were calculated using well known Arrhenius relation [36].

3.6 Impedance spectral analysis

Nowadays, complex impedance spectroscopy (CIS) mechanism is widely used to study structure-properties, bonding of the different types of materials, which comprises of ionic insulator, ferroelectric and linked ceramics in various experimental conditions [37]. In this mechanism, the corresponding phase shifted current response is obtained by an alternating voltage signal applied to a sample. The complex electrical parameters [real (′) and imaginary (″) parts] of impedance (Z), modulus (M), and permittivity (ε) can be determined with the help of the CIS technique.

Figure 6a, b exhibits the variation of Z′ and Z″ vs. frequency at various temperatures. The real (′) and imaginary (″) part of complex impedance can be drafted by following equation [38]:

$$Z' = \frac{R}{(1 + \omega\tau)^2} \text{ and } Z'' = \frac{\omega R\tau}{1 + (\omega\tau)^2} \tag{1}$$

where R represents resistance, ω represents angular frequency and the relaxation time is given by $\tau = RC$ (C = capacitance). The Z′ magnitude decreases with increasing temperature at low frequencies. The semiconductor behavior of material is indicated [39]. The presence and release of space charge depict the temperature dependent spectra are merged into one above a critical frequency [40]. With the increase in the temperature, Z″ decreases, showing
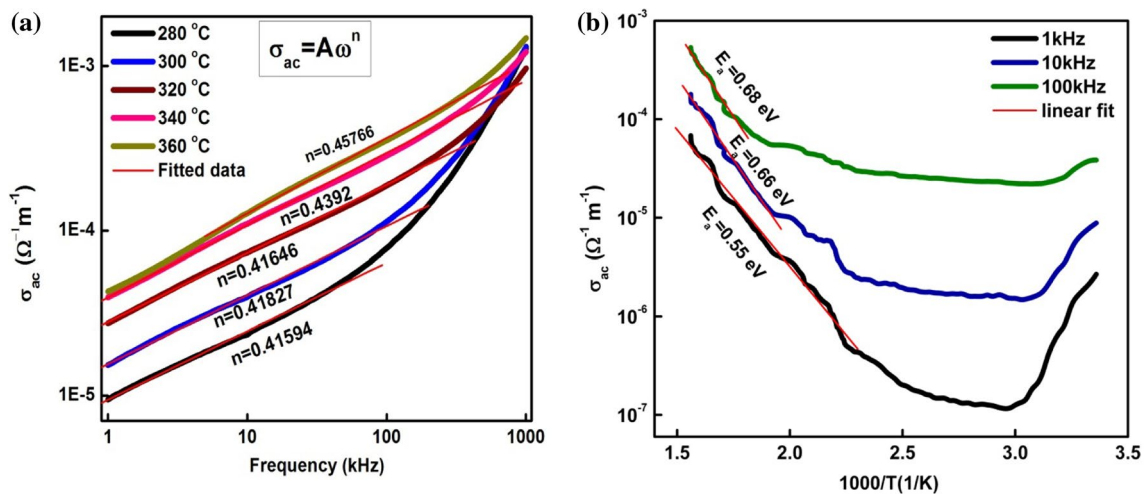

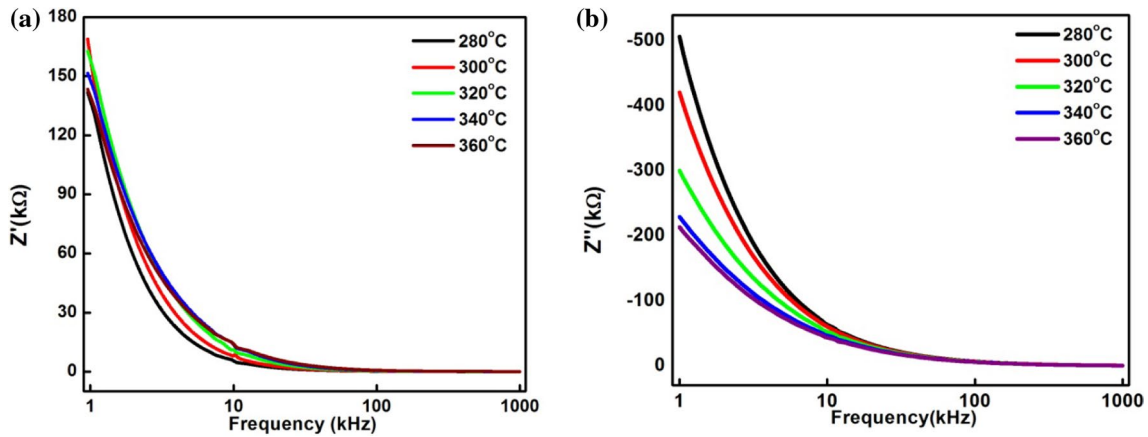**Fig. 5** **a** AC conductivity vs. frequency and **b** AC conductivity vs. temperature plot

Fig. 6 **a** Z′ vs. frequency and **b** Z″ vs. frequency at various temperatures (280–360 °C)
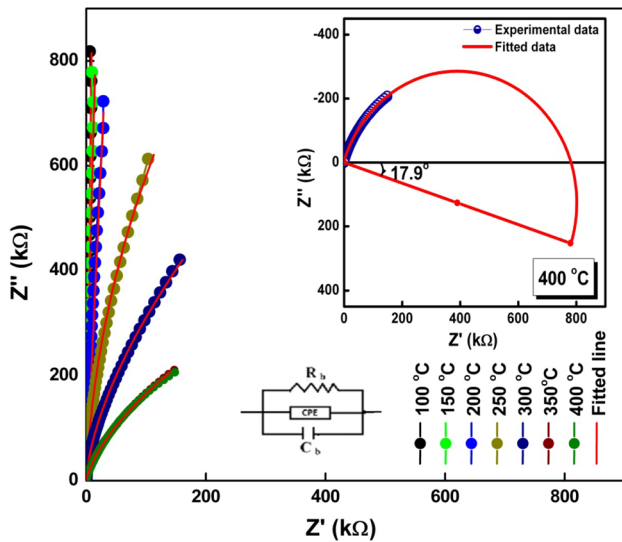

Fig. 7 Nyquist plots through experimental and fitted data along with inset equivalent circuit fitted in model

Table 1 Value of grain capacitance (C_g), grain resistance (R_g) and apparent bulk conductivity (σ_{dc}) for sample BNT–BT-2 at various temperatures

Temperature (°C)	R_g	C_g	$\sigma_{dc} = t/(R_b A)$
100	17.3×10^8	6.11×10^{-16}	1.14×10^{-8}
150	7.4×10^7	2.84×10^{-15}	2.66×10^{-7}
200	1.0×10^{15}	1.00×10^{-20}	1.97×10^{-14}
250	4.44×10^5	4.01×10^{-20}	4.44×10^{-5}
300	6.59×10^6	2.32×10^{-10}	2.99×10^{-6}
350	5.8×10^6	2.35×10^{-10}	3.40×10^{-6}
400	1.5×10^6	1.95×10^{-10}	1.31×10^{-5}

the presence of relaxation process in the material due to low-temperature immobility of species [41].

Figure 7 shows a temperature dependence of Nyquist plot (Z′ vs. Z″ plot) of the material studied. The relation at low temperatures between above components is linear which gradually converts to depressed semicircle with an increase in the temperature. The relaxation process is non-ideal or non-Debye type in the present sample, as the asymmetric arc center is depressed under the x-axis (Z′ axis) [42]. The factors responsible for the happening of non-Debye relaxation is size distribution grains, defect distribution, grain boundaries and orientation, the stress–strain phenomenon at the atomic level [43]. We add a constant phase element (CPE) in the model equivalent circuit for understanding the asymmetric or depressed nature of the semicircle and electrical

response of materials. The fitting curves (solid line) and numerical data of different equivalent circuit model elements were obtained using commercially available ZSIMP WIN version 2 software. It indicates that there is occurrence of grain effect. The value of resistance of the grain (R_g), the capacitance of grain (C_g) and DC conductivity was obtained and compared in Table 1 with the help of the fitted curve at various temperatures. From Table 1, we observed that there is both increase and decrease in the value of R_g with rise in temperature so in some temperature region it shows NTCR whereas in temperature region it shows PCTR behaviour [44].

3.7 Modulus analysis

Figure 8a indicates the change of M' with frequency for BNT–BT-2 in a wide temperature region (280–360 °C). It is observed that in the low-frequency region, M' approaches to zero and on increasing the frequency, there is a continuous dispersion. The reason behind such occurrence is the charge carriers with short range mobility and it contributed to the conduction mechanism. Under the
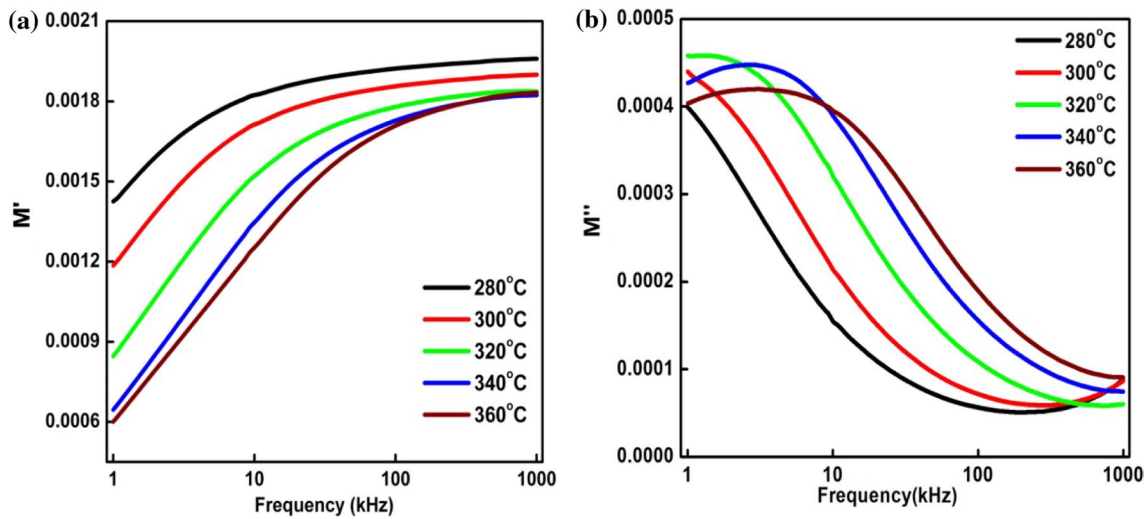
Fig. 8 a shows M′ vs. frequency and **b** M″ vs. frequency of BNT–BT-2 at various temperatures

effect of steady electric field, it shows lack of restoring force for charge flow [45]. The removal of electrode effect in the sample is confirmed.

It is observed in Fig. 8**b** with increase in temperature that the M'' shifts to the higher frequency. The asymmetric peak broadening ascribes non-Debye type relaxation that shows the distribution of relaxation times with various time constant. The movement of ions over a long distance is observed from low frequency peaks, whereas the high frequency peaks merge to ion confinement in a potential well. The existence of a hopping mechanism of conduction in material is depicted from the plot [46].

3.8 J–E characterization

Figure 9 indicates that with increase in E at various temperatures (200–290 °C), the value of J increases. The value of enhanced leakage current under higher electric field suggests the presence of a thermally assisted conduction process in the material. The above plot is nonlinear in nature which exhibits non-Ohmic characteristics like semiconductor [47]. This is mainly due to the reason of thermionic emission of electrons over barrier or may be the movement of electrons through barrier with decreasing width. Such type of characteristics cannot be explained by means of the Rose theory of exponential trap distribution and the Poole–Frenkel effect respectively. Hence, Parakht et al. [48] reported the non-Ohmic conduction in polycrystalline ceramics on basis of Rose theory of space charge limited currents (sclc) in defect insulators with shallow traps.
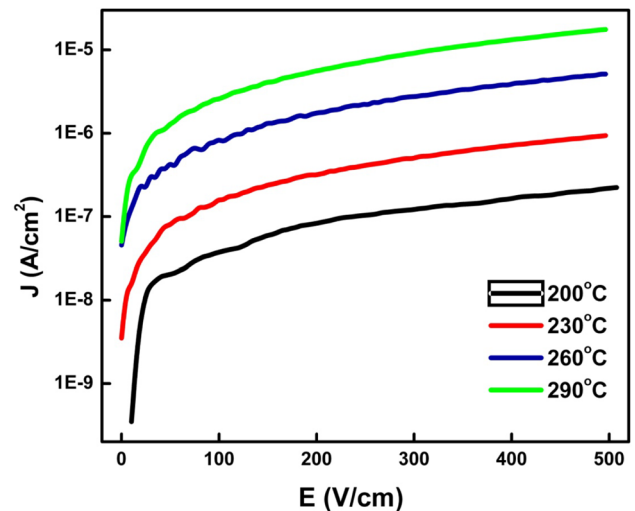

Fig. 9 J–E Characterization at various temperature zones

4 Conclusions

A lead-free BNT–BT-2 system at MPB was prepared by a mixed oxide route. The structure and electrical analysis have offered co-existence of hexagonal and tetragonal phases with high density non-uniform grain growth. The peak width, peak location and intensity were detected by Raman spectroscopy. The dielectric constant attains maximum limit with rise in temperature, and with further rise in temperature, it decreases. The temperature variation of two sharp anomalies near to 200 and 340 °C, are linked to the motion of domain walls. Due to the decrease in the porosity and dielectric loss, it highlights to a low loss material. The diffused parameter values also represent

relaxor type behavior in the sample. The non-Ohmic type conduction is basically obtained from J–E characteristics.

References

1. J. Rodel, W. Jo, T.P. Seifert, E.M. Anton, T. Granzow, D. Damjanovic, Perspective on the development of lead-free piezoceramics. J. Am. Ceram. Soc. **92**, 1153–1177 (2009)

2. A. Herabut, A. Safari, Processing and electromechanical properties of $(Bi_{0.5}Na_{0.5})$ (1-1.5x) La_xTiO_3 ceramics. J. Am. Ceram. Soc. **80**, 2954–2958 (1997)

3. T. Takenaka, Piezoelectric properties of some lead-free ferroelectric ceramics. Ferroelectrics **230**, 87–98 (1999)

4. X.J. Li, Q. Wang, Q.L. Li, Effects of MnO_2 addition on microstructure and electrical properties of $(Bi_{0.5}Na_{0.5})_{0.94}Ba_{0.06}TiO_3$ ceramics. J. Electroceram. **20**, 89–94 (2008)

5. K.S. Rao, H. Workineh, A. Swathi, B.S. Kalyani, Synthesis, piezoelectric, dielectric and conductivity studies on Dy_2O_3 substituted $(Bi_{0.94}Na_{0.94})_{0.5}Ba_{0.06}TiO_3$ ceramics. J. Adv. Dielectr. **1**, 455 (2011)

6. T. Takenaka, H. Nagata, Y. Hiruma, Current developments and prospective of lead-free piezoelectric ceramics. Jpn. J. Appl. Phys. **47**, 3787–3801 (2008)

7. P.K. Panda, Review: Environmental friendly lead-free piezoelectric materials. J. Mater. Sci. **44**, 5049–5062 (2009)

8. E. Aksel, J.L. Jones, Advances in lead-free piezoelectric materials for sensors and actuators. Sensors **10**, 1935–1954 (2010)

9. W.J. Merz, The electric and optical behavior of BaTiO3 single-domain crystals. Phys. Rev. **76**, 1221 (1949)

10. L. Egerton, D.M. Dillion, Piezoelectric and dielectric properties of ceramics in the system potassium-sodium niobate. J. Am. Ceram. Soc. **42**, 438–442 (1959)

11. R.E. Jaeger, L. Egerton, Hot pressing of potassium-sodium niobates. J. Am. Ceram. Soc. **45**, 209–213 (1962)

12. S. Ikegami, I. Ueda, Piezoelectricity in ceramics of ferroelectric bismuth compound with layer structure. Jpn. J. Appl. Phys. **13**, 1572 (1974)

13. T. Takenaka, K. Sakata, Grain orientation and electrical properties of hot-forged $Bi_4Ti_3O_{12}$ ceramics, Jpn. J. Appl. Phys. **19**, 31–39 (1980)

14. X.X. Wang, H.L.W. Chan, C.L. Choy, $(Bi_{0.5}Na_{0.5})_{0.94}Ba_{0.06}TiO_3$ lead-free ceramics with simultaneous addition of CeO_2 and La_2O_3. Appl. Phys. A **80**, 333–336 (2005)

15. B.J. Chu, D.R. Chen, G.R. Li, Q.R. Yin, Electrical properties of $Na_{1/2}Bi_{1/2}TiO_3$–$BaTiO_3$ ceramics. J. Eur. Ceram. Soc. **22**, 2115–2121 (2002)

16. H.D. Li, C.D. Feng, P.H. Xiang, Electrical properties of La^{3+} doped $(Na_{0.5}Bi_{0.5})_{0.94}Ba_{0.06}TiO_3$ ceramics. Jpn. Soc. Appl. Phys. **42**, 7387–7391 (2003)

17. C. Zhou, X. Liu, Dielectric and piezoelectric properties of $Bi_{0.5}Na_{0.5}TiO_3$-$BaNb_2O_6$ lead free piezoelectric ceramics. J. Mater. Sci. **19**, 29–32 (2008)

18. D. Lin. C. Xu, Q. Zheng, Y. Wei, D. Gao, Piezoelectric and dielectric properties of $Bi_{0.5}Na_{0.5}TiO_3$-$Bi_{0.5}Li_{0.5}TiO_3$ lead-free ceramics. J. Mater. Sci. **20**, 393–397 (2009)

19. B.V. Bahuguna Saradhi, K. Srinivas, G. Prasad, S.V. Suryanarayana, T. Bhimasankaram, Impedance spectroscopic studies inn ferroelectric $(Na_{1/2}Bi_{1/2})TiO_3$. Mater. Sci. Eng. B **98**, 10–16 (2003)

20. J. Suchanicz, Behavior of $Na_{0.5}Bi_{0.5}TiO_3$ ceramics in the as electric field. Ferroelectrics **209**, 561 (1998)

21. D. Lin, K.W. Kwok, Structure ferroelectric and piezoelectric properties of $(Bi_{0.98-x}La_{0.02}Na_{1-x})_{0.5}Ba_xTiO_3$ lead-free ceramics. Appl. Phys. A, **97**, 229–225 (2009)

22. K. Pengpat, S. Hanphimol, S. Eitssayeam, U. Intatha, G. Rujijanagul, T. Tunkasiri, Morphotropic phase boundary and electrical properties of lead-free bismuth sodium lanthanum titanate-barium titanate ceramics. J. Electroceram. **16**, 301–305 (2006)

23. S.R. McLaughlin, Fabrication and properties of $Bi_{1/2}Na_{1/2}TiO_3$ based ferroelectric ceramics with low levels of B-site additives. Ph.D. thesis, Queen's University, Kingston, Ontario, Canada, (2008)

24. J. Kreisel, A.M. Glazer, High-pressure Raman study of a relaxor ferroelectric: the $Na_{0.5}Bi_{0.5}TiO_3$ perovskite. Phys. Rev. B **63**, 174106–174110 (2001)

25. P. Tarte, A. Rulmont, M. Liégeois-Dyuckaerts, R. Cahay, J.M. Winand, Vibrational spectroscopy and solid state chemistry. Solid State Ionics **42**, 177–196 (1990)

26. J. Kreisel, A.M. Glazer, G. Jones, P.A. Thomas, L. Abello, G. Lucazeau, An X-ray diffraction and Raman spectroscopy investigation of A-site substituted perovskite compounds: the $(Na_{1-x}K_x)_{0.5}Bi_{0.5}TiO_3$ (0 = x = 1) solid solution. J. Phys. **12**, 3267–3280 (2000)

27. D. Rout, K.S. Moon, S.J.L. Kang, I.W. Kim, Dielectric and Raman scattering studies of phase transitions in the (100-x) $Na_{0.5}Bi_{0.5}TiO_3$-$xSrTiO_3$ System. J. Appl. Phys. **108**, 084102 (2010)

28. B.W.V. Eerd, D. Damjanovic, N. Klein, N. Setter, J. Trodahl, Structural complexity of $(Na_{0.5}Bi_{0.5})$ TiO_3-$BaTiO_3$ as revealed by Raman spectroscopy. Phys. Rev. B **82**, 104112(2010)

29. P.S. Dobal, A. Dixit, R.S. Katiyar, Z. Yu, R. Guo, A.S. Bhalla, J. Appl. Phys. **89**, 8085–8091 (2001)

30. A. Ullah, C.W. Ahn, A. Hussain, I.W. Kim, The effects of sintering temperature on dielectric, ferroelectric and electric field-induced strain of lead-free $Bi_{0.5}(Na_{0.78}K_{0.22})_{0.5}TiO_3$ piezoelectric ceramics synthesized by the sol-gel technique. Curr. Appl. Phys. **10**, 1367 (2010)

31. G.A. Smolenskii, V.A. Isupov, A.I. Agranovskaya, N.N. Krainik, New ferroelectrics of complex composition. Sov. Phys. Solid State **2**, 2651 (1961)

32. T. Takenaka, K. Maruyama, K. Sakata, $(Bi_{1/2}Na_{1/2})TiO_3$-$BaTiO_3$ system for lead-free piezoelectric ceramics. Jpn. J. Appl. Phys. **30**, 2236 (1991)

33. C. Xu, D. Lin, K.W. Kwok, Structure, electric properties and depolarization temperature of $(Bi_{0.5}Na_{0.5})TiO_3$-$BaTiO_3$ lead-free piezoelectric ceramics. Solid State Sci **10**, 934–940 (2008)

34. S. Sahoo, P.K. Mahapatra, R.N.P. Choudhary, M.L. Nandagoswami, A. Kumar, Structural, electrical and magnetic characteristics of improper multiferroic: $GdFeO_3$. Mater. Res. Express **3**, 065017 (2016)

35. S. Sahoo, P.K. Mahapatra, R.N.P. Choudhary, Effect of sintering temperature on dielectric, electrical and magneto-electric characteristics of chemico-thermally synthesized $(Ba_{0.9}Gd_{0.1})$ $(Ti_{0.9}Fe_{0.1})$ O_3. Ceram. Int. **42**, 15955–15967 (2016)

36. T. Acharya, R.N.P. Choudhary, Development of ilmenite- type electronic material $CdTiO_3$ for devices. IEEE Trans. Dielectr. Electr. Insul. **22**, 3521 (2015)

37. S. Maity, D. Bhattacharya, S.K. Ray, Structural and impedance spectroscopy of pseudo-co-ablated $(SrBi_2Ta_2O_9)_{(1-x)}$–$(La_{0.67}Sr_{0.33}MnO_3)_x$ composites. J. Phys. D **44**, 095403 (2011)

38. A. Rouahi, A. Kahouli, F. Challali, M.P. Besland, C. Vallée, B. Yangui, S. Salimy, A. Goullet, A. Sylvestre, Impedance and electric modulus study of amorphous TiTaO thin films: highlight of the interphase effect. J. Phys. D **46**, 065308 (2013)

39. M. Idrees, M. Nadeem, M.M. Hassan, Investigation of conduction and relaxation phenomena in $LaFe_{0.9}Ni_{0.1}O_3$ by impedance spectroscopy. J. Phys. D **43**, 155401 (2010)

40. A.R. James, C. Prakash, G. Prasad, Structural properties and impedance spectroscopy of excimer laser ablated Zr substituted $BaTiO_3$ thin films. J. Phys. D **39**, 1635 (2006)

41. C.K. Suman, K. Prasad, R.N.P. Choudhary, Complex impedance studies on tungsten-bronze electroceramic: $Pb_2Bi_3LaTi_5O_{18}$. J. Mater. Sci. **41**, 369 (2006)

42. S. Chatterjee, P.K. Mahapatra, R.N.P. Choudhary, A.K. Thakur, Complex impedance studies of sodium pyrotungstate—$Na_2W_2O_7$. Phys. Status Solidi **201**, 588 (2004)

43. S. Sen, R.N.P. Choudhary, A. Tarafdar, P. Pramanik, Impedance spectroscopy study of strontium modified lead zirconate titanate ceramics. J. Appl. Phys. **99**, 124114–124118 (2006)

44. D.K. Pradhan, R.N.P. Choudhary, C. Rinaldi, R.S. Katiyar, Effect of Mn substitution on electrical and magnetic properties of $Bi_{0.9}La_{0.1}FeO_3$. J. Appl. Phys. **106**, 024102–024110 (2009)

45. B.C. Sutar, R. Piyush, R.N.P. Das, Choudhary, Synthesis and electrical properties of $Sr(Bi_{0.5}V_{0.5})O_3$ electroceramic. Adv. Mater. Lett. **5**, 131–137 (2014)

46. J.R. Macdonald, Note on the parameterization of the constant-phase admittance element. Solid State Ionics **13**, 147–149 (1984)

47. T. Acharya, R.N.P. Choudhary, Structural, optical and electrical characteristics of a $La_{0.5}K_{0.5}Ga_{0.5}V_{0.5}O_3$ system. J. Electron. Mater. **45**, 947–958 (2016)

48. N.C. Parakht, J.C. Garg, Non-ohmic electric conduction in polycrystalline thulium oxide. Bull. Mater. Sci. **7**, 483–489 (1985)